

Production of the entire range of r -process nuclides by black hole accretion disc outflows from neutron star mergers

Meng-Ru Wu^{1*}, Rodrigo Fernández^{2,3}, Gabriel Martínez-Pinedo^{1,4},
Brian D. Metzger⁵

¹ *Institut für Kernphysik, Technische Universität Darmstadt, 64289 Darmstadt, Germany*

² *Department of Physics, University of California, Berkeley, CA 94720, USA*

³ *Department of Astronomy and Theoretical Astrophysics Center, University of California, Berkeley, CA 94720, USA*

⁴ *GSI Helmholtzzentrum für Schwerionenforschung, Planckstr. 1, 64291 Darmstadt, Germany*

⁵ *Department of Physics and Columbia Astrophysics Laboratory, Columbia University, New York, NY, 10027, USA*

Received / Accepted

ABSTRACT

We consider r -process nucleosynthesis in outflows from black hole accretion discs formed in double neutron star – black hole mergers. These outflows, powered by angular momentum transport processes and nuclear recombination, represent an important – and in some cases dominant – contribution to the total mass ejected by the merger. Here we calculate the nucleosynthesis yields from disc outflows using thermodynamic trajectories from hydrodynamic simulations, coupled to a nuclear reaction network. We find that outflows produce a robust abundance pattern around the second r -process peak (mass number $A \sim 130$), independent of model parameters, with significant production of $A < 130$ nuclei. This implies that dynamical ejecta with high electron fraction may not be required to explain the observed abundances of r -process elements in metal poor stars. Disc outflows reach the third peak ($A \sim 195$) in most of our simulations, although the amounts produced depend sensitively on the disc viscosity, initial mass or entropy of the torus, and nuclear physics inputs. Some of our models produce an abundance spike at $A = 132$ that is absent in the Solar system r -process distribution. The spike arises from convection in the disc and depends on the treatment of nuclear heating in the simulations. We conclude that disc outflows provide an important – and perhaps dominant – contribution to the r -process yields of compact binary mergers, and hence must be included when assessing the contribution of these systems to the inventory of r -process elements in the Galaxy.

Key words: accretion, accretion discs – dense matter – gravitational waves – nuclear reactions, nucleosynthesis, abundances – neutrinos – stars: neutron

1 INTRODUCTION

Approximately half of the elements with mass number $A > 70$, and all of the transuranic nuclei, are formed by the rapid neutron capture process (the r -process; Burbidge et al. 1957, Cameron 1957). The astrophysical site of this process has been under debate for more than 50 yrs (see, e.g., Qian & Wasserburg 2007, Arnould et al. 2007, Sneden et al. 2008, Thielemann et al. 2011 for reviews). Neutrino-driven outflows from proto neutron stars (NSs) following core collapse supernovae have for long been considered the prime candidate site (Meyer et al. 1992; Woosley et al. 1994; Qian & Woosley 1996). However, state-of-the-art calculations find thermodynamic conditions that are at best marginal for the r -process, especially when extending up to the heaviest third-peak elements with

mass number $A \sim 195$ (e.g. Martínez-Pinedo et al. 2012; Roberts et al. 2012; Martínez-Pinedo et al. 2014).

Prospects for a successful r -process in neutrino-driven outflows may be improved if the proto-NS is born with a strong magnetic field and very rapid rotation (e.g. Thompson et al. 2004; Metzger et al. 2007; Vlasov et al. 2014). If the supernova itself is MHD-powered, additional magnetocentrifugal acceleration could substantially reduce the electron fraction of the outflow compared to its value in the purely neutrino-driven case favouring the occurrence of an r -process (e.g. Burrows et al. 2007, Winteler et al. 2012, Nishimura et al. 2015). However, current simulations of MHD-powered supernova explosions need further improvements, especially considering the role of instabilities on the jet structure which manifest in three dimensions (Mösta et al. 2014).

The coalescence of double NS (NS–NS) and NS–black hole (NS–BH) binaries (Lattimer & Schramm 1974) provides an al-

* E-mail: mwu@theorie.ikp.physik.tu-darmstadt.de

ternative r -process source. Numerical simulations of these events show that a robust outcome of the merger is the ejection of $\sim 10^{-4}$ – $10^{-1} M_{\odot}$ of highly neutron-rich matter on the dynamical time (e.g. Hotokezaka et al. 2013, Bauswein et al. 2013; see Lehner & Pretorius 2014 and Baiotti & Rezzolla 2016 for recent reviews). Estimates show that NS–NS/NS–BH mergers could contribute a sizable fraction of the total production of r -process elements in the Galaxy, depending on the uncertain merger rates. At the same time, previous arguments against mergers being dominant r -process sites based on Galactic chemical evolution and the observed prompt enrichment of r -process nuclei in metal poor stars (e.g. Argast et al. 2004) have been challenged (e.g., van de Voort et al. 2015; Shen et al. 2015; Hirai et al. 2015). Additional evidence supporting the presence of a ‘high yield’ r -process site – like an NS–NS/NS–BH merger – includes the discovery of highly r -process enriched stars in the ultra-faint dwarf galaxy Reticulum II (Ji et al. 2016), and the abundance of the short-lived isotope ^{244}Pu on the sea floor (Wallner et al. 2015; Hotokezaka et al. 2015).

Nucleosynthesis in NS–NS/NS–BH mergers has also received a recent surge of interest due to the realization that the radioactive decay of the r -process ejecta can power a thermal transient (a ‘kilonova’; e.g., Li & Paczyński 1998, Metzger et al. 2010, Roberts et al. 2011, Barnes & Kasen 2013, Tanaka & Hotokezaka 2013), which could serve as a promising electromagnetic counterpart to the gravitational waves (Metzger & Berger 2012). The detection of a possible kilonova following the *Swift* GRB 130603B (Berger et al. 2013; Tanvir et al. 2013) highlights the potential of kilonovae as both a unique diagnostic of physical processes at work during the merger and a direct probe of the formation of r -process nuclei (see, e.g., Rosswog 2015, Fernández & Metzger 2016, Tanaka 2016 for recent reviews).

Previous work on the r -process in NS–NS/NS–BH mergers has been focused primarily on the dynamical ejecta that is unbound promptly during the immediate aftermath of the merger (e.g. Meyer 1989, Freiburghaus et al. 1999, Goriely et al. 2005). Earlier simulations that did not include weak interactions have shown this unbound matter to be highly neutron-rich, with an electron fraction $Y_e \lesssim 0.1$, sufficiently low to produce a robust abundance pattern for heavy nuclei with $A \gtrsim 130$ as the result of fission cycling (e.g., Goriely et al. 2011, Korobkin et al. 2012, Bauswein et al. 2013, Mendoza-Temis et al. 2015). More recently, a number of merger calculations that include the effects of e^{\pm} captures and neutrino irradiation in full general-relativity have shown that the dynamical ejecta can have a wider electron fraction distribution ($Y_e \sim 0.1$ – 0.4) than models without weak interaction effects (Sekiguchi et al. 2015; Foucart et al. 2015; Radice et al. 2016). As a result, lighter r -process elements with $90 \lesssim A \lesssim 130$ are generated in addition to third-peak elements (Wanajo et al. 2014). It is important to keep in mind, however, that the light element yields in these calculations are dependent on the assumed dense-matter equation of state and on the details of the neutrino transport employed, in addition to the NS radii and the binary mass ratio.

In addition to ejecting material dynamically, NS–NS/NS–BH mergers result in the formation of an accretion disc around the central remnant (e.g., Oechslin & Janka 2006); with the latter being a promptly formed BH or a longer-lived hypermassive NS (HMNS) (e.g., Shibata & Uryū 2000). In both cases, the accretion disc can generate outflows on time-scales much longer than the orbital time (e.g., Metzger et al. 2008; Lee et al. 2009; Metzger et al. 2009), and with a contribution to the total mass ejection that can be comparable to, or even larger than that from the dynamical ejecta (Fig/ 1, see also Fernández & Metzger 2016). A relatively massive disc

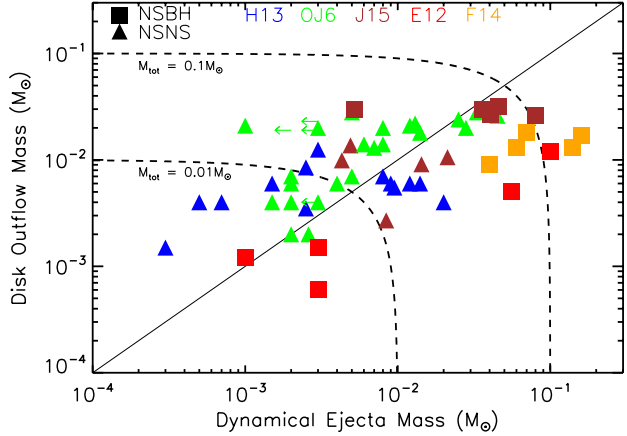


Figure 1. Mass ejected dynamically during a compact binary merger versus that ejected in disc outflows. Each point corresponds to the result of a single time-dependent NS–NS (triangles) and BH–NS (squares) simulation. Shown are models by Hotokezaka et al. (2013) (blue), Oechslin & Janka (2006) (green, upper limits shown by arrows), Just et al. (2015) (brown), East et al. (2012) (red), and Foucart et al. (2014) (orange). The mass unbound in disc outflows is estimated to be 10 per cent of the mass of the remnant disc, based on calculations of the subsequent accretion disc evolution (e.g., FM13). Dashed lines show total ejecta mass contours (dynamical + disc winds) of $0.01 M_{\odot}$ and $0.1 M_{\odot}$, bracketing the range necessary to explain the Galactic production rate of heavy r -process nuclei $\sim 5 \times 10^{-7} M_{\odot} \text{ yr}^{-1}$ (Qian 2000), given the allowed range of the rates of NS–NS mergers $\in [4, 61] \text{ Myr}^{-1}$ (99% confidence) calculated based on the population of Galactic binaries (Kim et al. 2015). In reality, the ejecta mass range required to reproduce the Galactic abundances is uncertain by greater than an order of magnitude, due to systematic uncertainties on the merger rate and depending on the precise atomic mass range under consideration (e.g., Bauswein et al. 2014). See also Fernández & Metzger (2016).

($\sim 0.1 M_{\odot}$) can be formed following a NS–NS merger, as part of the process by which the HMNS sheds angular momentum outwards prior to collapsing into a BH (e.g. Shibata & Taniguchi 2006). Long-term hydrodynamic simulations of the disc evolution show that a significant fraction of the initial disc mass (~ 5 – 20% , corresponding to $\sim 0.01 M_{\odot}$) is unbound in outflows powered by heating from angular momentum transport and nuclear recombination, on a timescale of $\gtrsim 1$ s (Fernández & Metzger 2013, hereafter FM13; Just et al. 2015, Fernández et al. 2015). As the result of weak interactions, the electron fraction of the disc outflows lies in the range $Y_e \sim 0.2$ – 0.4 , generally higher than that of the dynamical ejecta, but still sufficiently low to achieve the r -process (Just et al. 2015).

Although most of the previous work on merger disc wind nucleosynthesis has focused on parametrized outflows powered by neutrino heating (e.g. McLaughlin & Surman 2005; Surman et al. 2008; Caballero et al. 2012; Surman et al. 2014), in analogy with proto-NS winds, time-dependent models of the long-term disc evolution show that neutrino heating is sub-dominant relative to viscous heating in driving most of the disc outflow when a BH sits at the centre (FM13, Just et al. 2015). Neutrino heating is much more important if the merger produces a long-lived HMNS (Dessart et al. 2009; Metzger & Fernández 2014; Perego et al. 2014; Martin et al. 2015), resulting in a larger ejecta mass with higher electron fraction, depending on the uncertain lifetime of such a remnant. To date, the only fully time-dependent nucleosynthesis study of long-term outflows from BH accretion discs was carried out by Just et al. (2015), who found that disc outflows can generate elements from

$A \sim 80$ to the actinides, with the contribution above $A = 130$ being sensitive to system parameters.

In this paper we further investigate nucleosynthesis in the outflows from NS–NS/NS–BH merger remnant accretion discs around BHs, by applying a nuclear reaction network on thermodynamic trajectories extracted from fully time-dependent, long-term hydrodynamic simulations of disc outflows. Our aim is to carry out a systematic study of the dependence of the *r*-process production on system parameters such as disc mass or viscosity, and on additional ingredients such as nuclear physics inputs to the reaction network or the feedback from nuclear heating on the disc dynamics. Our main conclusion is that disc outflows from NS binary mergers can in principle produce both the light and heavy *r*-process elements, without necessarily requiring additional contributions from the dynamical ejecta.

The paper is organized as follows. Section 2 describes the hydrodynamic models, extraction of thermodynamic trajectories, and the properties of the nuclear reaction network. Results and analysis are presented in section 3. Finally, section 4 summarizes our findings and discusses broader astrophysical implications.

2 COMPUTATIONAL METHOD

2.1 Disc evolution and thermodynamic trajectories

We evolve NS merger remnant accretion discs around BHs using the approach described in FM13, Metzger & Fernández (2014), and Fernández et al. (2015). The equations of hydrodynamics are solved numerically using FLASH3 (Fryxell et al. 2000; Dubey et al. 2009). The public version of the code has been modified to include the equation of state of Timmes & Swesty (2000) with abundances of nucleons and α particles (^4He) in nuclear statistical equilibrium (NSE), angular momentum transport due to an α viscosity (Shakura & Sunyaev 1973), and the pseudo-Newtonian potential of Artemova et al. (1996). In addition, neutrino emission and absorption due to charged-current weak interactions on nucleons are included through energy- and lepton number source terms using a leakage scheme for cooling and a disc-adapted lightbulb approach for self-irradiation, with simple optical-depth corrections (see FM13 and Metzger & Fernández 2014 for details).

Discs start from an equilibrium initial condition and are evolved in axisymmetric spherical polar coordinates over thousands of orbits at the initial density maximum (physical time of several seconds). The majority of the mass loss is produced once the disc reaches the advective state, in which viscous heating and nuclear recombination forming α particles are unbalanced by neutrino cooling (Metzger et al. 2009). Heating due to neutrino absorption makes only a minor contribution to the total mass ejection if a BH sits at the centre (FM13, Just et al. 2015). Total ejected masses can range from a few percent to more than $\sim 20\%$ of the initial disc mass for a highly-spinning BH.

Thermodynamic trajectories of the outflow are obtained by inserting passive tracer particles in the hydrodynamic simulations. For each model, 10^4 equal mass particles are initially placed in the disc with random positions that follow the mass distribution (Fig. 2a). Each particle records thermodynamic variables including density, temperature, electron fraction and nucleon abundances, as well as neutrino and viscous source terms. Some of these quantities are used as input for the *r*-process nuclear reaction network (§2.3), while others are retained to check for consistency.

In order to assess the effects of additional nuclear heating after

Table 1. Hydrodynamic disc models evolved. Columns from left to right are: initial torus mass, black hole mass, radius of initial torus density peak, initial electron fraction, initial entropy, viscosity parameter, BH spin parameter, and amplitude of parametrized nuclear heating (equation 6).

Model	M_{10}	M_{BH}	R_0	Y_{e0}	s_0	α	χ	ε
	(M_\odot)		(km)		(k_B/b)			
S-def	0.03	3	50	0.10	8	0.03	0	0
$\chi 0.8$							0.8	
m0.01	0.01	3	50	0.10	8	0.03	0	0
m0.10	0.10							
r75	0.03	3	75					
M10		10	150					
y0.05		3	50	0.05				
y0.15				0.15				
s6				0.10	6			
s10					10			
$\alpha 0.01$					8	0.01		
$\alpha 0.10$						0.10		
$\varepsilon 1.0$	0.03	3	50	0.10	8	0.03	0	1.0
$\varepsilon 0.1$								0.1
$\varepsilon 10.0$								10.0

the α -recombination on the disc dynamics, we carry out a few simulations in which we include this extra source term. This heating is parametrized analytically as a function of temperature by analysing an ensemble of trajectories in our baseline model (§3.4).

Relative to the BH accretion disc models of FM13, we have corrected an error in the treatment of the nuclear binding energy of α particles (as described in Metzger & Fernández 2014), which results in slightly lower mass ejection than reported in FM13. Since Fernández et al. (2015) we have also corrected an error in the computation of the charged-current weak interaction rates, whereby the neutron-proton mass difference was missing in the argument of the Fermi-Dirac integrals of the neutrino rates but not the antineutrino rates (e.g., Bruenn 1985). After correcting this error, we obtain a slightly less neutron rich outflow distribution, with a tail towards higher Y_e . Nonetheless the average properties of the outflow remain relatively unchanged.

2.2 Models Evolved

Table 1 presents all the models studied in this paper. Following FM13, the baseline configuration (model S-def) consists of a BH with mass $M_{\text{BH}} = 3M_\odot$, and an equilibrium torus with disc mass $M_{10} = 0.03M_\odot$, radius at density peak $R_0 = 50$ km, constant specific angular momentum, constant initial entropy $s_0 = 8$ k_B per baryon, constant electron fraction $Y_{e0} = 0.1$, viscosity parameter $\alpha = 0.03$ and BH spin $\chi = 0$. We also include a model ($\chi 0.8$) with BH spin parameter $\chi = 0.8$ to bracket the range of outcomes expected for an NS–NS merger.

The remaining models vary one parameter at a time, mirroring the simulations in FM13. In addition, we evolve three models that include nuclear heating after α recombination in the hydrodynamics (§2.1). All models are evolved for 3000 orbits measured at R_0 , which amounts to several seconds of physical time, in order to approach convergence in mass ejection (the disc material left over interior to $r = 2 \times 10^9$ cm amounts to a few percent of the initial disc mass).

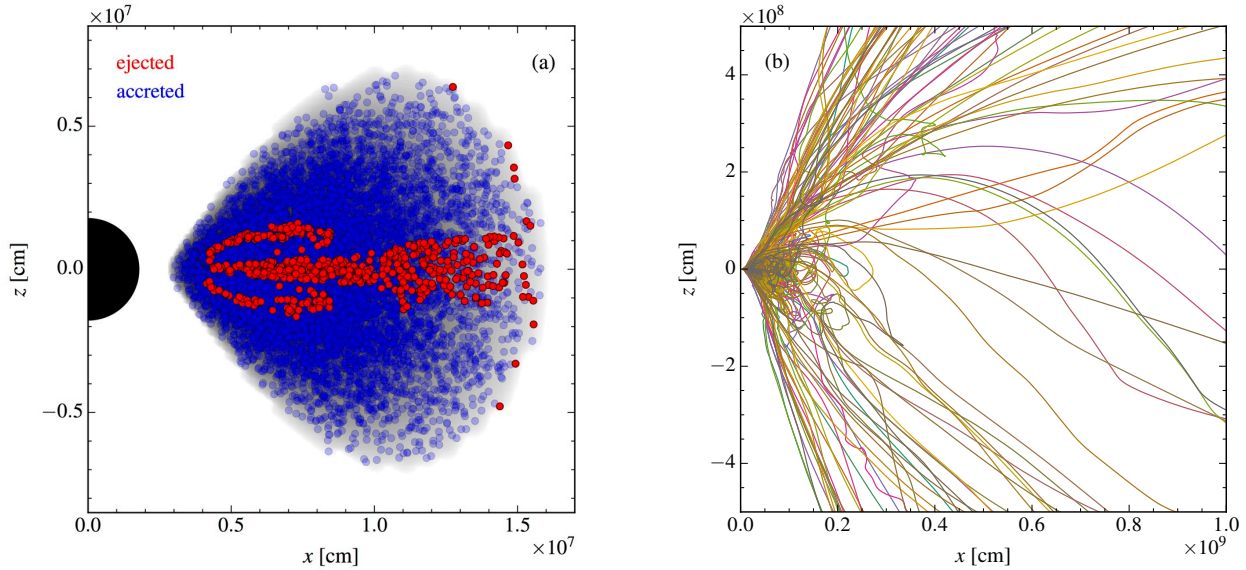


Figure 2. Left: initial density field (grey) and particle distribution in model S-def. Particles that reach a distance of 2×10^9 cm from the BH are considered to be ejected (red), with most of the remainder being accreted (blue). Right: paths followed by ejected particles, showing the convective character of the disc outflow (only 20% of the outflow trajectories are shown, for clarity).

2.3 Nuclear Reaction Network

The initial disc temperature is of the order of a few MeV, so that nearly all the ejecta consist initially of neutrons and protons. Once the temperature drops to ~ 10 GK, most of the free protons recombine with neutrons to form ${}^4\text{He}$, as favoured by NSE under neutron-rich conditions ($Y_e \sim 0.2$). The nuclear binding energy released by forming ${}^4\text{He}$ plays an important role in unbinding the material and is included in the hydrodynamic simulations as described in Sec. 2.1.

In order to follow the change in abundances of nuclear species in the disc outflow, we use a large nuclear reaction network for all tracer particles that reach a distance of 2×10^9 cm from the centre of the BH. The nuclear reaction network includes 7360 nuclei from nucleons to ${}^{313}\text{Ds}$, and reaction rates including α -decays, β -decays, charged-particle reactions, neutron captures and their inverse photo-dissociation interactions, as well as spontaneous, β -delayed, and neutron-induced fission and the corresponding fission yields (see Mendoza-Temis et al. 2015, for a detailed description of the nuclear physics input used). In addition, we include charged-current neutrino interactions on free nucleons as described in Sec. 2.1.

For each tracer particle, we start the network calculation from the last moment when the temperature equals 10 GK. For a small fraction ($\lesssim 10\%$) of the particles the temperature is always below 10 GK, because they are initially located at the outer edge of the disc (e.g. Fig. 2a). For these particles, we instead follow the nucleosynthesis evolution from the beginning of the disc simulation. The initial composition of each trajectory is determined by NSE given the temperature, density, and Y_e . The density evolution is obtained at early times by interpolating the values provided by the simulation. Once the network evolution reaches the end of the disc simulation time t_f , we assume homologous expansion such that $\rho(t) = \rho(t_f) \times (t_f/t)^3$ subsequently. The temperature evolution is interpolated from the simulation as long as the temperature satisfies $T > T_s \equiv 6$ GK. For $T < T_s$, the temperature is evolved with the network following the same method used in Freiburghaus et al.

(1999) by including the energy sources from the viscous and the neutrino heating for $t < t_f$ provided by the hydrodynamic simulations, and the nuclear energy release due to reactions calculated directly by the network. We have checked that the final overall abundances are not sensitive to the choice of T_s . This suggests that, differently to what happens in dynamical ejecta, r -process heating in disc ejecta does not strongly influence the abundances because the total energy released by this channel is much smaller than the internal energy of the ejecta. This is consistent with the findings of Just et al. (2015). However, we discuss in Sec. 3.4 the potential impact of nuclear heating on the disc dynamics and on specific abundance features.

Since the r -process typically involves the nuclear physics properties of very neutron-rich nuclei that are not experimentally known, the outcome of nucleosynthesis calculations is subject to theoretical uncertainties in the modelling of these properties. In the case of dynamical ejecta, it has been shown that both the neutron-capture and β -decay rates can substantially influence the positions and heights of the r -process peaks (e.g., Mendoza-Temis et al. 2015, Eichler et al. 2015). Our standard set of calculations uses neutron-capture and photo-dissociation rates based on nuclear masses from the Finite Range Droplet Model (FRDM) (Möller et al. 1995) supplemented by the β -decay rates of Möller et al. (2003) for all disc models listed in Table 1. To address the so far unexplored impact of nuclear physics on disc ejecta, we have performed calculations using neutron capture and photodissociation rates based on the Duflo–Zuker mass model with 31 parameters (DZ31; Duflo & Zuker 1995) and β -decay rates from Marketin et al. (2016), see Sec. 3.5.

3 RESULTS

Neutrino cooling in the disc is strong during the first ~ 10 – 100 ms, largely balancing viscous heating. As the disc spreads, neutrino cooling shuts off and energy deposition by viscous heating and α recombination make the disc highly convective. The resulting out-

flow peaks on a time-scale of ~ 1 s, measured at a large enough radius that a significant fraction of the material will become gravitationally unbound from the system upon expansion ($r \sim 10^9$ cm). Weak interactions drive Y_e towards its equilibrium value, which in the inner disc can be as high as ~ 0.4 . However, most of this material is accreted on to the BH. The bulk of the wind material arises from regions of the disc midplane and on its back side relative to the BH (Fig. 2a), and are thus only moderately influenced by neutrino interactions. A component close to the BH at high altitude is mixed into the wind, increasing the average electron fraction, particularly when the BH spin is high (Fernández et al. 2015).

During the initial expansion at high temperature ($10 \text{ GK} \gtrsim T \gtrsim 5 \text{ GK}$), charged-particle reactions dominate the nucleosynthetic flow to form seed nuclei. At $T \approx 5 \text{ GK}$, seed nuclei abundances peak at $A \approx 50$ ($N \approx 30$) and $A \approx 80$ ($N \approx 50$). Heavier nuclei are only synthesized when $T \lesssim 5 \text{ GK}$ by subsequent neutron capture processes and β -decays. Given the importance of this temperature threshold, it is useful to examine different quantities when this point is reached. For each trajectory, we denote the value of a given quantity X at $T = 5 \text{ GK}$ by

$$X_5 \equiv X \Big|_{T=5 \text{ GK}}. \quad (1)$$

If $T = 5 \text{ GK}$ is reached multiple times due to convective motions (Fig. 2b), X_5 is chosen as the value at the last time when $T = 5 \text{ GK}$. It is also informative to measure quantities in the disc outflow at large radius, where the effects of the BH and convection are less likely to affect the properties of the outflow. We thus denote the value of a given quantity X at $r = 10^9$ cm by

$$X_9 \equiv X \Big|_{r=10^9 \text{ cm}}. \quad (2)$$

Finally, we denote the average of a quantity over all trajectories by

$$\bar{X}_s \equiv \frac{\sum_i X_{s,i}}{N}, \quad (3)$$

where N is the total number of trajectories, i labels each trajectory, and the subscript s can be 5 or 9. Note that since all trajectories have the same mass, this is a mass average.

3.1 Ejecta properties and nucleosynthesis in the baseline model

The *r*-process abundance distribution obtained with the baseline model S-def is shown in Fig. 3. A breakdown of the thermodynamic- and kinematic properties of the ejecta as a function of various quantities is illustrated in Fig. 4. The particle-averaged properties are also summarized in Table 2. The disc outflow has a broad distribution of electron fraction spanning the range $0.1 \leq Y_{e,5} \leq 0.4$, with a mean at $\bar{Y}_{e,5} \approx 0.24$. The entropy peaks at $s_5 = 10 \text{ k}_B$ per baryon, with a long tail extending out to $\sim 30 \text{ k}_B$ per baryon, and the neutron-to-seed ratio $R_{n/s,5}$ lies in the range 20–100. In terms of kinematics, most of the outflow reaches 5 GK within 2 s and its angular distribution peaks at $\sim \pm 45^\circ$ – 60° from the disc equatorial plane. Ejecta velocities lie in the range $(0.2\text{--}1.6) \times 10^9 \text{ cm s}^{-1}$, much slower than the typical values for the early phase of the dynamical ejecta (see, e.g., Just et al. 2015). With such a broad distribution of $Y_{e,5}$, the resulting average nucleosynthetic abundances are in overall agreement with the Solar system *r*-process distribution from $A \sim 80$ to U and Th, as shown in Fig. 3, despite a large spread among individual trajectories.

In order to clarify the origin of the spread in abundances for individual particles, we bin trajectories into intervals of electron

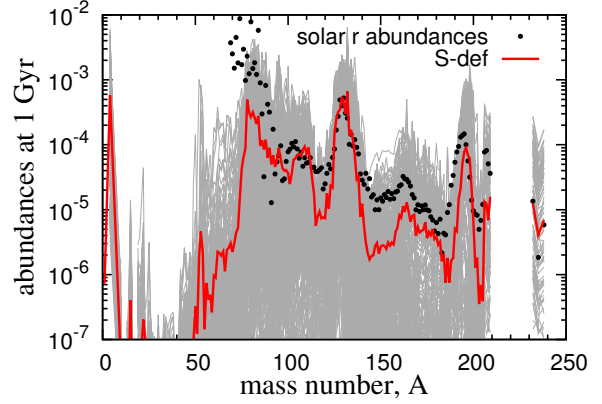


Figure 3. Abundances at 1 Gyr as a function of mass number A for the baseline model S-def. Shown are the average abundances over all trajectories (thick red curve) and results for individual particles (thin grey curves). Black dots show the Solar system *r*-abundances (Cowan et al. 1999) scaled to match the averaged abundances around the second peak.

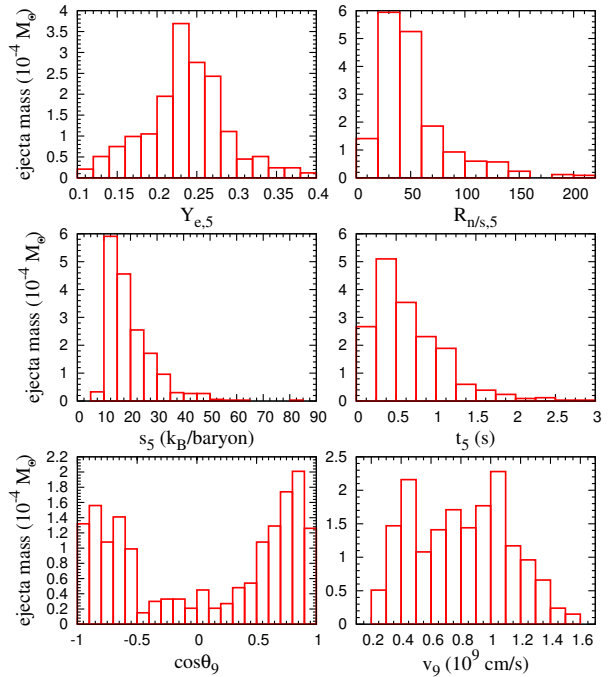


Figure 4. Mass distribution of the disc outflow from the baseline model S-def, as a function of electron fraction $Y_{e,5}$, neutron-to-seed ratio $R_{n/s,5}$, entropy s_5 , time t_5 , polar angle θ_9 , and radial velocity v_9 . Subscripts have the meanings defined in equations (1) and (2).

fraction $Y_{e,5}$, entropy s_5 , time t_5 , polar angle θ_9 , and radial velocity v_9 , with the results shown in Fig. 5. The nucleosynthesis results are most sensitive to the electron fraction (see Fig. 5a). Most of the abundances above the rare-Earth peak ($A \gtrsim 150$) come from ejecta with $Y_{e,5} \leq 0.2$. Trajectories with $Y_{e,5}$ in the range 0.1–0.3 contribute to the production of the second peak ($A \approx 130$). As for the abundances around $A \lesssim 110$, they are dominantly from the ejecta with $Y_{e,5} \gtrsim 0.25$. Fission plays a role only for ejecta with $Y_e \lesssim 0.15$ and consequently represents a minor contribution to the final abundances.

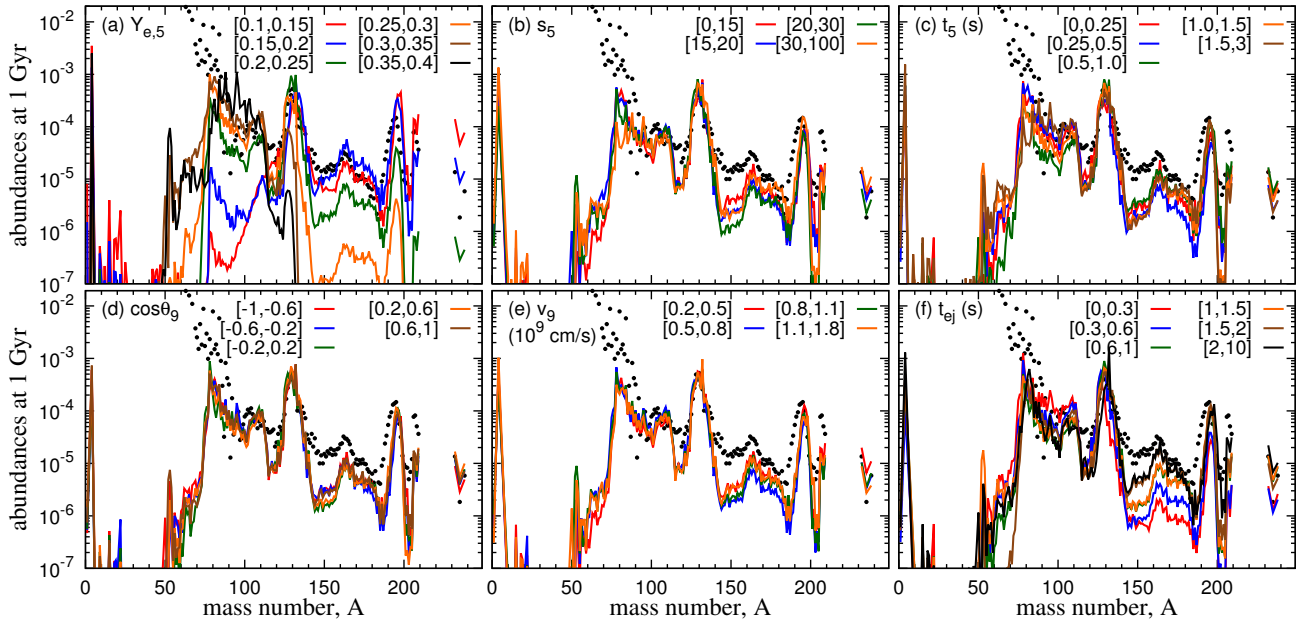


Figure 5. Dependence of the abundances on different ejecta properties, for the baseline model S-def. Each panel shows average abundances as a function of mass number, binned into intervals of the variable shown in the upper-left corner: electron fraction (a), entropy (b), time at $T = 5$ GK (c), polar angle (d), radial velocity (e), and ejection time (f), with subscripts defined in equations (1) and (2). The interval values are shown in the corresponding legends.

Interestingly, the nucleosynthesis outcome is not sensitive to the entropy intervals in the ejecta as shown in Fig. 5b. This is mainly because the different entropy bins have nearly the same electron fraction distribution, with only a minor trend of lower entropy having lower peaked $Y_{e,5}$ distributions. As a result, we do not recover the entropy dependence obtained in parametrized nucleosynthesis studies such as Lippuner & Roberts (2015). The abundance patterns are rather insensitive to other quantities such as the polar angle θ_9 of each particle (see Fig. 5c-e).

The disc outflow is strongly convective out to late times (Fig. 2b), unlike the ejecta from the neutrino-driven wind in core-collapse supernovae or the dynamical ejecta of NS-NS/NS-BH mergers, for which the density and temperature of the ejecta monotonically decrease as the medium expands. Particles in the disc outflow may in fact go through several convective cycles before being ejected at temperatures of ~ 1 GK. To quantify the effect of this process on the nucleosynthesis, we define the ejection time t_{ej} of each particle as the time in the simulation after which the radial position only increases monotonically with time. This quantity is shown in Fig. 6 as a function of t_5 for all particles in the S-def model, with each point colored by the electron fraction $Y_{e,5}$.

Fig. 6 clarifies several aspects of the ejecta behaviour. First, there is a substantial amount of material having much larger t_{ej} than t_5 for $t_5 \lesssim 1$ s. Before ejection, these particles are subject to strong convective motions in low-temperature regions ($T < 5$ GK) at a late phase in the disc evolution. Secondly, the electron fraction $Y_{e,5}$ of trajectories ejected at the earlier times is higher. This occurs because neutrino irradiation plays a larger role in unbinding this early ejecta and thus naturally raises its $Y_{e,5}$ to higher values. Consequently, the rare-earth and third peak abundances are much lower for matter being ejected at earlier time than for later ejecta, as shown in Fig. 5f. In particular, the abundance of Lanthanides can differ by almost a factor of 10 compared to the latest particles. This is consistent with the results of Fernández et al. (2015), who

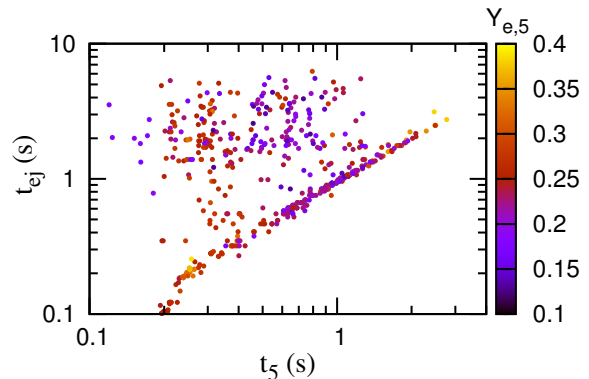


Figure 6. Ejection time t_{ej} as a function of time t_5 (equation 1), for all trajectories from the baseline model S-def. Each point is colored by the electron fraction at time t_5 .

on the basis of the Y_e distribution of the ejecta suggested that the wind contains a Lanthanide-free “skin” – even in the case of a non-spinning BH – which can generate a small amount of blue optical emission if not obstructed by neutron-rich dynamical ejecta (Kasen et al. 2015).

Note also that a very strong $A = 132$ abundance spike around the second peak is formed for ejecta with $2.0 < t_{ej} < 10$ s. This feature and its relation to convective motions is the subject of §3.3.

3.2 Dependence on model parameters

The effect of changing various disc parameters on the average nucleosynthetic abundances of the outflow is shown in Fig. 7 and summarized in Table 2. We note that the Solar system r -abundances

Table 2. Average ejecta properties for models listed in Table 1. Columns from left to right show model name, electron fraction, entropy, time, expansion timescale $\tau_{\text{exp}} = \bar{r}/\bar{v}_r$, radius, velocity, final average mass number, percentage of ejected mass, percentage of ejected tracer particles that contain both $Y_{A=132} > 10^{-3}$ and $Y_{A=128(136)} < 0.1 Y_{A=132}$, and the total mass fraction of lanthanides and actinides ($57 \leq Z \leq 71$ and $89 \leq Z \leq 103$), $X_{\text{Lan+Act}}$, at $t = 1$ d. Subscripts and averages are defined in equations (1)-(3). Only trajectories that reach $r = 2 \times 10^9$ cm at the end of the simulation are considered.

Model	$\bar{Y}_{e,5}$	\bar{s}_5 (k_B/b)	\bar{t}_5 (s)	$\bar{\tau}_{\text{exp},5}$ (ms)	\bar{r}_5 (10^7 cm)	$\bar{v}_{r,9}$ 10^9 cm s $^{-1}$	$\langle \bar{A} \rangle_f$	M_{ej}/M_{t0} %	132-peak %	$X_{\text{Lan+Act}}$ %
S-def	0.237	19.9	0.65	81	3.84	0.81	119	5.67	11.8	4.30
$\chi 0.8$	0.282	19.9	0.81	82	4.56	1.04	103	18.05	13.2	2.01
m0.01	0.202	20.4	0.43	89	3.18	0.91	137	5.32	16.5	8.32
m0.10	0.261	19.1	1.04	104	4.90	0.93	109	5.00	10.6	3.02
M10	0.228	20.2	0.53	227	6.48	0.62	119	6.29	24.2	5.49
r75	0.231	17.6	0.77	117	4.94	0.73	122	14.80	22.3	5.40
s10	0.260	18.8	0.60	91	4.29	0.75	107	7.19	16.4	2.34
s6	0.203	20.8	0.73	96	3.75	0.86	136	4.22	13.0	0.91
$\alpha 0.01$	0.321	26.1	2.66	100	2.88	0.70	91	1.36	0	0.25
$\alpha 0.10$	0.206	18.1	0.16	52	4.56	1.23	130	13.53	2.2	8.85
y0.05	0.230	20.5	0.72	110	3.93	0.91	122	5.00	13.6	5.12
y0.15	0.252	19.4	0.66	102	4.44	0.87	112	5.72	19.2	3.26
$\epsilon 1.0$	0.230	14.9	0.41	111	4.28	0.85	118	11.39	5.1	4.40
$\epsilon 0.1$	0.228	17.5	0.58	95	3.90	0.77	122	6.08	15.3	4.77
$\epsilon 10.0$	0.216	14.5	0.28	131	4.24	2.38	123	16.11	0	5.09

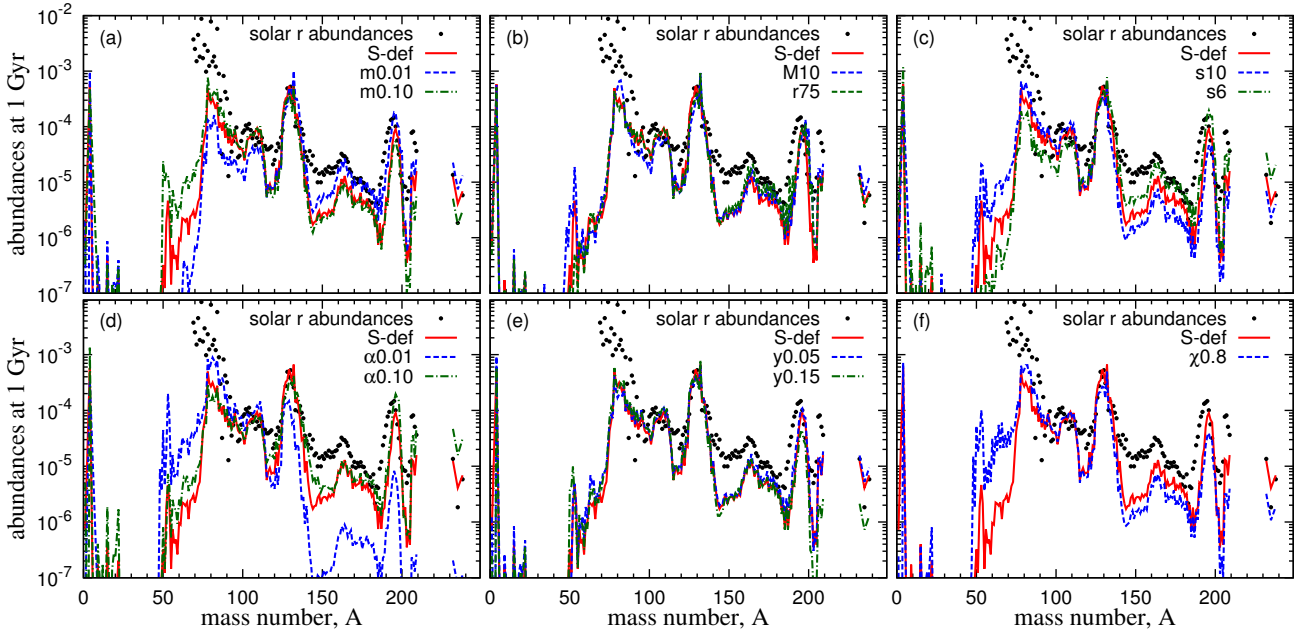


Figure 7. Dependence of average disc outflow abundances on disc mass (a), BH mass and disc radius (b), initial entropy (c), viscosity parameter (d), initial electron fraction (e), and BH spin (f). Model parameters are shown in Table 1, with nucleosynthesis results summarized in Table 2. Note that the Solar system r -abundances are scaled to match the second peak abundances of S-def model only. When comparing to abundances of other models, they should be further re-scaled.

shown in Fig. 7 are scaled to match the second peak abundances of S-def model only. When comparing to abundances of other models, they should be further re-scaled.

The largest impact of changing disc parameters is obtained when varying the α viscosity parameter (see Fig. 7d). Since the disc evolution timescale is governed by the viscous time $t_{\text{visc}} \propto \alpha^{-1}$, models with lower (higher) viscosity have a longer (shorter) \bar{t}_5 relative to the S-def model. The corresponding $\bar{Y}_{e,5}$ is raised to higher

(lower) values by weak interactions. As a result, model $\alpha 0.10$ ($\bar{Y}_{e,5} = 0.206$) has about a factor of 2 higher abundances of third peak and heavier elements compared to S-def ($\bar{Y}_{e,5} = 0.237$). At the other end, model $\alpha 0.01$ ($\bar{Y}_{e,5} = 0.321$) displays a relatively large first peak ($A \approx 80$) while the abundances at and above the second peak are reduced by roughly an order of magnitude.

The initial disc mass and entropy have a moderate impact (see Fig. 7a and c). For discs with initially larger (smaller) entropy, the

temperature is higher (lower). As a result, higher (lower) positron capture rates give rise to a higher (lower) value of $\bar{Y}_{e,5}$. Similarly, for a disc with initially larger (smaller) mass, $\bar{Y}_{e,5}$ is also higher (lower) because the disc temperature is higher (lower) for fixed entropy, disc radius, and BH mass due to the higher (lower) density. Smaller changes are obtained when varying the initial electron fraction (see Fig. 7e). Higher (lower) initial Y_e leads to a slightly larger (smaller) third peak and trans-lead abundances. This insensitivity originates in the fact that, while the outflow itself does not achieve β -equilibrium (c.f. Fig. 6 of Fernández & Metzger 2013), weak interactions nonetheless modify Y_e significantly from its initial value.

Regarding BH spin, a higher value of this parameter results in a smaller innermost stable circular orbit, leading to more gravitational energy release in the form of neutrinos and viscous heating (e.g., Fernández et al. 2015). As a result, $\bar{Y}_{e,5}$ is higher in model $\chi 0.8$ than in the baseline S-def model, slightly hindering the nucleosynthesis of heavy nuclei for both the second and third peaks while enhancing the first peak abundances as shown in Fig. 7f.

Changing the mass of the BH and radius of the disc do not lead to significant differences given our parameter choices. Fig. 7b shows that there are minor differences between models M10 and S-def. The similarities between them can be attributed to the very similar compactness, $M_{\text{BH}}/R_0 = 0.07$ and $0.06M_\odot \text{ km}^{-1}$ for M10 and S-def, respectively, which should correlate with the disc temperatures (and thus strength of weak interactions) if the medium is in near hydrostatic equilibrium. In contrast, model r75 has a somewhat lower compactness $0.04M_\odot \text{ km}^{-1}$ and shows a slightly larger abundance of elements with $A > 130$.

The dependence of the ejecta mass distribution on flow quantities – such as polar angle and velocity – for models with different parameters is generally similar to that for the baseline model S-def shown in Fig. 4.

We conclude that some nucleosynthesis features – particularly abundances of elements with $A \lesssim 130$ – are quite robust against variations in astrophysical disc parameters. On the other hand, the abundances of rare-earth peak, third peak and heavier elements are more sensitive to those parameters that alter either the disc evolution time-scale or the temperature.

3.3 Anomalously high abundance of $A = 132$

Fig. 7 shows that all models we have explored, except $\alpha 0.01$ and $\alpha 0.10$, display a peculiarity in the abundances at the second peak: the abundance of $A = 132$ elements ($Y_{A=132}$) exceeds that of the second Solar system r -process peak at $A = 128 - 130$ ($Y_{A=128-130}$). We find that this spike in $Y_{A=132}$ arises primarily from late-time ejecta (see, e.g., Fig. 5f). Table 2 shows that material satisfying $Y_{A=132} > 10^{-3}$ and $Y_{A=128(136)} < 0.1Y_{A=132}$ can contribute more than 10% to the total ejected mass. This would cause a discrepancy with the observed solar abundance ratio $Y_{A=132}/Y_{A=130} \approx 0.5$ if we were to assume that the disc ejecta dominates the galactic r -process production of second peak elements.

The origin of this anomaly can be traced back to late-time, low-temperature convection in the disc outflow. For ejecta satisfying $t_{\text{ej}} \gg t_5$, neutron-capture processes operate once the temperature decreases to $\lesssim 2-3$ GK. Once neutrons are exhausted, the produced nuclei at $N = 82$, mainly isotones with $A = 128-130$, start to decay to the stability valley. If convection brings matter back to regions of $T \gtrsim 2-3$ GK on time-scales shorter than the half-lives of long lived Sn isotopes: ^{128}Sn ($t_{1/2} = 59.07$ min), ^{129}Sn ($t_{1/2} = 2.23$ min), and ^{130}Sn ($t_{1/2} = 3.42$ min), additional neutron

captures can occur due to the release of neutrons by photodissociation. This results in a pile up of material in the double-magic nucleus ^{132}Sn that itself has a β -decay half-life of $t_{1/2} = 39.7$ s.

The model with the smallest viscosity parameter ($\alpha 0.01$) does not display this anomaly because on one hand, the strength of convection is strongly reduced relative to the baseline value. Correspondingly, most of the ejecta from this model satisfy $t_{\text{ej}} \sim t_5$. On the other hand, most of the ejecta in this model contains $Y_{e,5} \gtrsim 0.25$ so that little nuclei with $A > 130$ can be produced. At the opposite end, the model with the highest viscosity ($\alpha 0.10$) also displays a much smaller abundance anomaly than S-def. In this case, if the viscous time is shorter than the r -process time scale $\lesssim 1$ s, each convection episode results in an incomplete r -process that does not use all available neutrons. Only the very last ejection episode results in a complete r -process. Therefore, only little trajectories contain the abundance anomaly.

The above discussion illustrates the close interplay between convection and r -process nucleosynthesis. Convection operating on time-scales longer than the r -process time-scale of $\lesssim 1$ s will reheat the r -process products during their decay back to stability and produce anomalies in the abundance distribution.

3.4 Effect of nuclear heating

The hydrodynamic disc models discussed so far do not self-consistently include the nuclear energy released by charged-particle reactions involving nuclei heavier than ^4He , in addition to the energy released by the r -process. These contributions are only included in post-processing with the nuclear network and hence can only affect the temperature. Charged-particle reactions can release a nuclear energy ~ 3 MeV/nucleon through processes like $20\text{n} + 15\alpha \rightarrow ^{80}\text{Zn}$. This can give rise to a heating rate $\sim 10^{19}$ erg s^{-1} , assuming that such reactions occur on a time-scale of ~ 0.1 s. It can become comparable to the viscous heating rate in the same temperature regime, and has the potential to change not only the nucleosynthesis but also the disc dynamics. The energy released during the r -process is smaller in comparison, amounting to $\sim 10^{18}$ erg s^{-1} , but can potentially also play a role at late times. Given the abundance anomaly discussed in the previous section, and its sensitivity to convection in the disc, we explore here the extent to which additional sources of heating can introduce changes in the dynamics and nucleosynthesis results.

In order to include these additional heating channels into hydrodynamic models, we have parametrized it out of trajectories from the S-def model using a method similar to that described in Just et al. (2015). From our post-processed nucleosynthesis calculation, we estimate the particle-averaged nuclear heating rate $\langle \dot{q} \rangle$ as a function of the average temperature $\langle T \rangle$ by calculating

$$\langle \dot{q}(\bar{t}) \rangle \equiv \frac{\sum_i \dot{q}_i(\bar{t})}{N} \quad (4)$$

and

$$\langle T(\bar{t}) \rangle \equiv \frac{\sum_i T_i(\bar{t})}{N}, \quad (5)$$

where $\dot{q}_i(\bar{t}) = \dot{q}_i(t - t_{0,i})$ and $T_i(\bar{t}) = T_i(t - t_{0,i})$ are the nuclear energy generation rate and temperature of each trajectory i , respectively, and $t_{0,i}$ is the time at which the network integration begins for each trajectory (§2.3). Following Korobkin et al. (2012), we find that the function $\langle \dot{q} \rangle(\langle T \rangle)$ can be approximated by

$$\langle \dot{q} \rangle(\langle T \rangle) = 2.5 \times 10^{19} \varepsilon \left[\frac{1}{\pi} \arctan \left(\frac{\langle T \rangle}{1.1 \text{ GK}} \right) \right]^{5/2} \text{ erg g}^{-1} \text{ s}^{-1}, \quad (6)$$

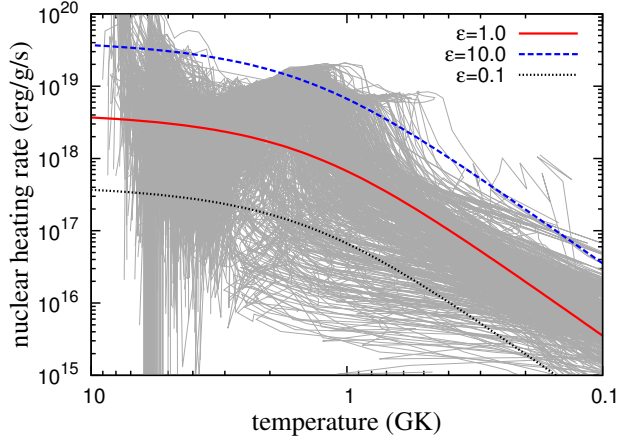


Figure 8. Nuclear heating rate as a function of temperature for all trajectories from the baseline model S-def (grey curves). Also plotted is an analytic fit to the average heating rate (equation 6) for three choices of the heating amplitude ε , as shown in the legend.

with $\varepsilon \approx 1.0$. Fig. 8 compares the result from equation (6) with the heating rates from individual particles in the S-def model.

We evolve three additional hydrodynamic models that include this additional heating rate using a range of values for the heating amplitude $\varepsilon = \{0.1, 1, 10\}$ to compensate for the crudeness of the approximation (models $\varepsilon 0.1$, $\varepsilon 1.0$ and $\varepsilon 10.0$ in Table 1). The heating term is added to the energy equation once $T \leq 6$ GK if $v_r > 0$. The latter condition is used to prevent heating in flows that move back towards the BH.

Table 2 shows that the additional heating can enhance the ejected mass up to a factor of 2 when using $\varepsilon \gtrsim 1.0$. The angular distribution can also be affected. In the model $\varepsilon 10.0$, the mass ejection becomes more isotropic rather than peaks at high latitudes.

Nucleosynthesis results are shown in Fig. 9. The abundances of third peak and heavier elements are slightly increased relative to the baseline model S-def. Interestingly, the $A = 132$ abundance anomaly is reduced in model $\varepsilon 1.0$ and completely vanishes in model $\varepsilon 10.0$, as shown in the inset of Fig. 9. For the $\varepsilon 1.0$ model, this suppression occurs because the disc evolution becomes faster as a result of the extra heating, so that the amount of late-time ejecta affected by convection is reduced. For model $\varepsilon 10.0$, the nuclear heating is so strong that convection is strongly suppressed.

Our results indicate that including all nuclear heating sources may be necessary to fully understand the ejecta dynamics and the details of the nucleosynthesis outcome. Alternatively, the dynamics of the disc when transporting angular momentum via magnetohydrodynamic stresses might be different enough to erase the $A = 132$ abundance anomaly without the need for enhanced nuclear heating. The properties of convective motion in a purely hydrodynamical α -disc may differ substantially from those of MHD turbulence (e.g., Balbus & Hawley 2002).

3.5 Impact of nuclear physics input

In order to explore the effect of varying the nuclear physics inputs on the outflow nucleosynthesis, we have performed two additional network calculations on the baseline model S-def using different neutron-capture and photo-dissociation rates, as well as β -decay rates. Alternative neutron capture and photodissociation rates are computed with the nuclear mass model of Duflo-Zuker with 31 pa-

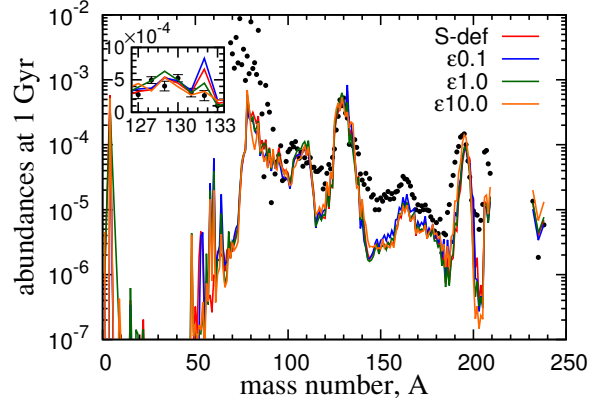


Figure 9. Dependence of the average disc outflow abundances on the amplitude ε of the parametrized radioactive heating rate (equation 6), relative to the baseline model S-def (c.f. Table 1). The inset shows the amplitude of the anomalous abundance peak at $A = 132$ in comparison with the solar r -abundances including observational uncertainties.

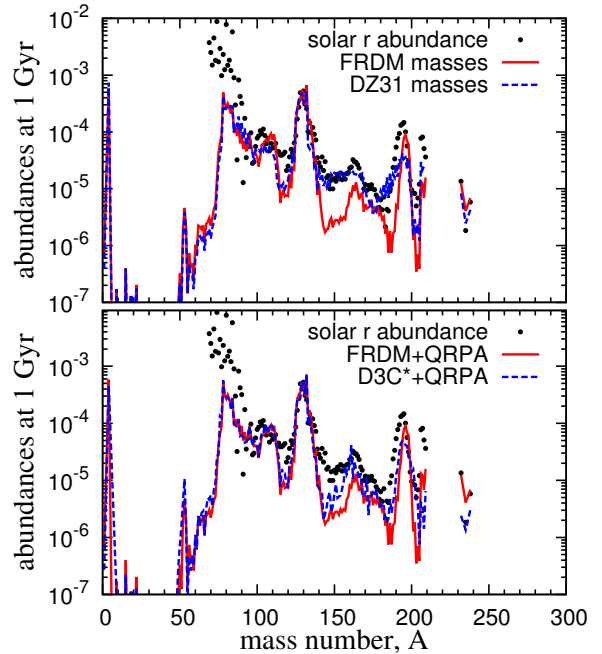


Figure 10. Average abundances in the outflow from the baseline model S-def for different nuclear mass models (top) and β -decay rates (bottom). See §3.5 for details.

rameters (DZ31; Duflo & Zuker 1995), as in Mendoza-Temis et al. (2015). To explore the impact of β -decay rates, we alternatively employ those of Marketin et al. (2016) and Möller et al. (2003).

The results of these additional calculations are shown in Fig. 10. The first and second r -process peaks are robust against changes in nuclear physics inputs, as they are produced primarily by trajectories with high $Y_{e,s}$, whose nucleosynthesis paths are close to the stability valley. For these trajectories, the relative change of neutron separation energy is small between the different mass models, and the predictions from two sets of β -decay rates are similar. In contrast, nuclear physics inputs can strongly affect the abundances

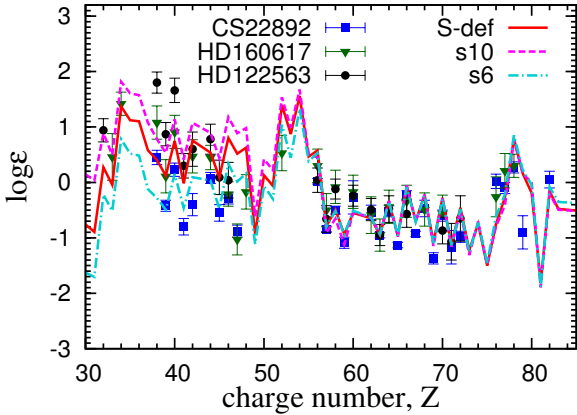


Figure 11. Comparison of average elemental abundances in the outflows from the baseline model S-def and models with different initial entropy (s6 and s10) to observed abundances in three metal-poor stars: CS22892-052 (Sneden et al. 2003), HD160617 (Roederer & Lawler 2012), and HD122563 (Roederer et al. 2012). Abundances are re-scaled to the Eu abundance of CS22892-052. Here $\log \varepsilon(Z) = \log(N_Z/N_1) + 12$, where N_Z is the abundance of an element with charge number Z .

of rare-earth and third peak elements – produced by low $Y_{e,5}$ ejecta – to a similar or even larger degree than the change due to astrophysical parameters discussed in §3.2. In particular, the troughs after the $A \sim 130$ peak and before the $A \sim 195$ peak may be due to deficiencies in the FRDM mass model (Winteler et al. 2012). A more detailed analysis of the effect of nuclear physics inputs will be reported separately.

3.6 Comparison with abundances of metal-poor stars

We have thus far restricted the comparison of disc nucleosynthesis abundances to the Solar system r -process distribution. Observations of r -process abundances in metal poor stars ($[\text{Fe}/\text{H}] = \log(N_{\text{Fe}}/N_{\text{H}}) - \log(N_{\text{Fe}}/N_{\text{H}})_{\odot} \lesssim -2.5$) suggest that the r -process operated at early times in the Galaxy (Sneden et al. 2008). While a number of metal-poor stars show robust relative abundances in the region around the rare-Earth peak ($56 \lesssim Z \lesssim 72$) that are similar to the solar r -abundance distribution, larger relative variations exist among lighter elements ($30 \lesssim Z \lesssim 50$). Moreover, the ratio between light-to-heavy elemental abundances can vary from star to star by more than a factor of 10. This has led to suggestions of the existence of more than one astrophysical site producing the r -process elements in the early Galaxy (Qian & Wasserburg 2007; Sneden et al. 2008).

Fig. 11 shows the comparison of elemental abundances from three models (S-def, s6, s10) to the observed abundances in three metal-poor stars: CS22892-052 (Sneden et al. 2003), HD160617 (Roederer & Lawler 2012), and HD122563 (Honda et al. 2006, Roederer et al. 2012), normalized to the Eu abundance of CS22892-052. These three stars show large differences in the ratio of light-to-heavy elemental abundances. If we consider disc outflows alone, changing the initial entropy of the disc can lead to qualitative agreement with the observations in these three metal-poor stars across the whole range of neutron capture elements. As shown in Sec. 3.2, changing other disc parameters such as the initial disc mass or the adopted α -viscosity can also result in similar or larger changes in abundances. This suggests that if the initial conditions in NS-NS/NS-BH mergers lead to variations in the remnant configura-

tions, the resulting disc outflows may account for different observed ratios of light and heavy elemental r -process abundances in metal poor stars. Therefore, the observed variations may not only be due to different combinations of dynamical and disc ejecta (as suggested by Just et al. 2015), but may arise due to variations of the merger remnant disc properties.

4 SUMMARY AND DISCUSSION

We have studied the production of r -process elements in the disc outflows from remnant accretion tori around BHs formed in NS-NS/NS-BH mergers. We used tracer particles in long-term, time dependent hydrodynamic simulations of these discs to record thermodynamic and kinematic quantities. The resulting trajectories were then post-processed with a dynamic r -process nuclear reaction network. Our results can be summarized as follows:

1. – Outflows from merger remnant discs around BHs can robustly generate light r -process elements with $A \lesssim 130$, regardless of the astrophysical parameters of the disc or the nuclear physics inputs employed (Fig. 5, Table 2).
2. – The yield of elements with $A > 130$ is most sensitive to the type and magnitude of the angular momentum transport process (Fig. 7d) and on the nuclear physics inputs employed in the nuclear reaction network (Fig. 10). Given the physics employed in our hydrodynamic models, the α viscosity parameter is a key factor determining the abundance of third peak and heavier elements. Other parameters such as the disc mass or initial entropy have a relatively smaller impact on the abundances.
3. – We have identified a spike in the abundance of $A = 132$ elements that arises whenever the disc outflow is highly convective, as is the case when using reasonable choices for the disc parameters (Fig. 5f). This feature can be erased if the disc evolution is fast or if the heating rate in the disc is very low, so that convection is suppressed.
4. – Inclusion of energy deposition from charged-particle reactions beyond ${}^4\text{He}$ recombination can affect the ejecta dynamics and nucleosynthesis to the point where the $A = 132$ abundance anomaly disappears (Fig. 9). Alternatively, the processes responsible for controlling angular momentum transport and the thermodynamics of the disc (e.g. MHD and neutrino transport) can have a sensitive nucleosynthetic impact. The properties of convective motions in an hydrodynamical α -disc may differ substantially from those of MHD turbulence (Balbus & Hawley 2002).
5. – The comparison with abundances observed in metal-poor stars shows that if the disc outflows contribute dominantly to the NS-NS/BS-BH ejecta, different initial configurations of the disc may account for the variation of light-to-heavy abundance ratio seen in these stars.

Our results together with those of Just et al. (2015) show that disc outflows are fundamental to understand r -process nucleosynthesis in mergers. For cases in which little dynamical ejecta is generated, *the disc outflow alone can contribute substantially to the heavy r -process element enrichment*, even while producing proportionally more elements with $A < 130$. This result reinforces the general view that NS-NS/NS-BH mergers are the primary astro-

physical site for heavy *r*-process elements. It is also important because the presence of high- Y_e dynamical ejecta in NS-NS mergers is uncertain theoretically, due in part to the dependence of shock-heated polar ejecta on the NS radius and equation of state.

The early ejection of material with high Y_e in the disc outflow has the potential to generate a blue peak in the kilonova, since it will generally reside on the outer layers of the ejecta (Fernández et al. 2015; Kasen et al. 2015). This nonetheless depends on the viewing directions close to the rotation axis to be relatively free of Lanthanide-rich dynamical ejecta material, which is usually the case for BH-NS mergers (Fernández et al. 2015; Kasen et al. 2015).

The net kilonova contribution of systems studied is Lanthanide-rich, as inferred from Table 2. The work of Kasen et al. (2013) shows that even a mass fraction of $\sim 10^{-2}$ in Lanthanides can increase the optical opacity by at least an order of magnitude relative to that of iron-like elements. Nearly all of our models have a Lanthanide mass fraction bigger than 1% and thus while an outer Lanthanide-free “skin” is usually obtained, the bulk of the wind will lead to an infrared transient. More promising in this respect is the possible onset of a neutron-powered precursor if a small fraction of material escapes quickly enough to freeze-out before neutrons are captured by heavy seeds (Metzger et al. 2015). Simulations at much higher resolution than currently available are needed to resolve this question. A long-lived NS remnant can also increase the quantity of high- Y_e ejecta, producing a more prominent blue component of the kilonova (Metzger & Fernández 2014).

A crucial improvement to our calculation would involve obtaining trajectories from an accretion disc outflow in which angular momentum transport – and the associated energy dissipation – is carried out by MHD stresses. Such a calculation can differ from ours in a number of ways. First, the change in the entropy due to viscous heating in an α -viscosity model is likely different in an MHD disc, with the associated change in the equilibrium Y_e that the weak interactions try to achieve. Secondly, the amount of mass ejected and the associated Y_e distribution can change, altering the relative amounts of heavy- and light *r*-process elements in the outflow composition. Finally, the kinematic properties of the wind can change, in particular the velocity, which controls the expansion time, and the angular distribution, which is associated with the level of neutrino irradiation of the ejecta (material on the equatorial plane is more effectively shadowed from neutrinos than material leaving at high latitudes).

Our calculations would also benefit from better neutrino transport, although the magnitude of the difference introduced can be comparable to that due to the spin of the BH (e.g., compare the results of Fernández et al. 2015 and Just et al. 2015). A more thorough, self-consistent treatment of nuclear heating would also make our calculations more realistic. In this respect, it is worth noting that the results of Just et al. (2015) do not appear to show the abundance spike at $A = 132$ that we obtain in many of our models. We surmise that this difference arises due to their inclusion of a single species of heavy nucleus (^{54}Mn) in the equation of state, which partially accounts for the energy production beyond α formation.

Finally, it is important to consider the combined evolution of disc and dynamical ejecta in computing the net *r*-process yield from NS-NS/NS-BH mergers. Part of the dynamical ejecta is gravitationally bound, and mixes with the accretion disc, increasing the neutron-richness of the disc and therefore lowering the peak of the Y_e distribution of the disc outflow (Fernández et al. 2015).

ACKNOWLEDGEMENTS

We gratefully thank Lutz Huther for his help during the initial stage of this work. We also thank Almudena Arcones, Kenta Hotokezaka for helpful discussions, Friedel Thielemann, Andreas Bauswein, Thomas Janka, Oliver Just, Luciano Rezzolla, Luke Roberts, and Ian Roederer for their valuable comments. MRW and GMP acknowledge support from the Deutsche Forschungsgemeinschaft through contract SFB 1245, the Helmholtz Association through the Nuclear Astrophysics Virtual Institute (VH-VI-417), and the BMBF-Verbundforschungsprojekt number 05P15RDFN1. RF acknowledges support from the University of California Office of the President, and from NSF grant AST-1206097. BDM gratefully acknowledges support from NASA grants NNX15AU77G (Fermi), NNX15AR47G (Swift), and NNX16AB30G (ATP), NSF grant AST-1410950, and the Alfred P. Sloan Foundation. The software used in this work was in part developed by the DOE NNSA-ASC OASCR Flash Center at the University of Chicago. This research used resources of the National Energy Research Scientific Computing Center (repository m2058), which is supported by the Office of Science of the U.S. Department of Energy under Contract No. DE-AC02-05CH11231. Some computations were performed at *Carver* and *Edison*. This research also used the *Savio* computational cluster resource provided by the Berkeley Research Computing program at the University of California, Berkeley (supported by the UC Berkeley Chancellor, Vice Chancellor of Research, and Office of the CIO).

REFERENCES

- Argast D., Samland M., Thielemann F.-K., Qian Y.-Z., 2004, *A&A*, 416, 997
- Arnould M., Goriely S., Takahashi K., 2007, *Phys. Rep.*, 450, 97
- Artemova I. V., Bjoernsson G., Novikov I. D., 1996, *ApJ*, 461, 565
- Baiotti L., Rezzolla L., 2016, preprint (arXiv:1607.03540)
- Balbus S. A., Hawley J. F., 2002, *ApJ*, 573, 749
- Barnes J., Kasen D., 2013, *ApJ*, 775, 18
- Bauswein A., Ardevol Pulpillo R., Janka H. T., Goriely S., 2014, *Astrophys. J.*, 795, L9
- Bauswein A., Goriely S., Janka H.-T., 2013, *ApJ*, 773, 78
- Berger E., Fong W., Chornock R., 2013, *ApJL*, 774, L23
- Bruenn S. W., 1985, *ApJS*, 58, 771
- Burbidge E. M., Burbidge G. R., Fowler W. A., Hoyle F., 1957, *Rev. Mod. Phys.*, 29, 547
- Burrows A., Dessart L., Livne E., Ott C. D., Murphy J., 2007, *ApJ*, 664, 416
- Caballero O. L., McLaughlin G. C., Surman R., 2012, *ApJ*, 745, 170
- Cameron A. G. W., 1957, *PASP*, 69, 201
- Cowan J. J., Pfeiffer B., Kratz K. L., Thielemann F. K., Sneden C., Burles S., Tytler D., Beers T. C., 1999, *Astrophys. J.*, 521, 194
- Dessart L., Ott C. D., Burrows A., Rosswog S., Livne E., 2009, *ApJ*, 690, 1681
- Dubey A., Antypas K., Ganapathy M. K., Reid L. B., Riley K., Sheeler D., Siegel A., Weide K., 2009, *J. Par. Comp.*, 35, 512
- Duflo J., Zuker A. P., 1995, *Phys. Rev. C*, 52, R23
- East W. E., Pretorius F., Stephens B. C., 2012, *Phys. Rev. D*, 85, 124009
- Eichler M., et al., 2015, *Astrophys. J.*, 808, 30
- Fernández R., Kasen D., Metzger B. D., Quataert E., 2015, *MNRAS*, 446, 750

- Fernández R., Metzger B. D., 2013, *MNRAS*, 435, 502
- Fernández R., Metzger B. D., 2016, *ARNPS*, 66, 2115
- Fernández R., Quataert E., Schwab J., Kasen D., Rosswog S., 2015, *MNRAS*, 449, 390
- Foucart F., Deaton M. B., Duez M. D., O'Connor E., Ott C. D., Haas R., Kidder L. E., Pfeiffer H. P., Scheel M. A., Szilagy B., 2014, *Phys. Rev. D*, 90, 024026
- Foucart F., O'Connor E., Roberts L., Duez M. D., Haas R., Kidder L. E., Ott C. D., Pfeiffer H. P., Scheel M. A., Szilagy B., 2015, *Phys. Rev. D*, 91, 124021
- Freiburghaus C., Rosswog S., Thielemann F., 1999, *ApJ*, 525, L121
- Fryxell B., Olson K., Ricker P., Timmes F. X., Zingale M., Lamb D. Q., MacNeice P., Rosner R., Truran J. W., Tufo H., 2000, *ApJS*, 131, 273
- Goriely S., Bauswein A., Janka H.-T., 2011, *ApJ*, 738, L32
- Goriely S., Demetriou P., Janka H.-T., Pearson J. M., Samyn M., 2005, *Nucl. Phys. A*, 758, 587
- Hirai Y., Ishimaru Y., Saitoh T. R., Fujii M. S., Hidaka J., Kajino T., 2015, *ApJ*, 814, 41
- Honda S., Aoki W., Ishimaru Y., Wanajo S., Ryan S. G., 2006, *Astrophys. J.*, 643, 1180
- Hotokezaka K., Kiuchi K., Kyutoku K., Okawa H., Sekiguchi Y.-I., Shibata M., Taniguchi K., 2013, *Phys. Rev. D*, 87, 024001
- Hotokezaka K., Piran T., Paul M., 2015, *Nature Physics*, 11, 1042
- Ji A. P., Frebel A., Chiti A., Simon J. D., 2016, *Nature*, 531, 610
- Just O., Bauswein A., Pulpillo R. A., Goriely S., Janka H.-T., 2015, *MNRAS*, 448, 541
- Kasen D., Badnell N. R., Barnes J., 2013, *ApJ*, 774, 25
- Kasen D., Fernández R., Metzger B. D., 2015, *MNRAS*, 450, 1777
- Kim C., Perera B. B. P., McLaughlin M. A., 2015, *MNRAS*, 448, 928
- Korobkin O., Rosswog S., Arcones A., Winteler C., 2012, *MNRAS*, 426, 1940
- Lattimer J. M., Schramm D. N., 1974, *ApJL*, 192, L145
- Lee W. H., Ramirez-Ruiz E., López-Cámara D., 2009, *ApJ*, 699, L93
- Lehner L., Pretorius F., 2014, *ARA&A*, 52, 661
- Li L., Paczyński B., 1998, *ApJ*, 507, L59
- Lippuner J., Roberts L. F., 2015, *Astrophys. J.*, 815, 82
- Marketin T., Huther L., Martínez-Pinedo G., 2016, *Phys. Rev. C*, 93, 025805
- Martin D., Perego A., Arcones A., Thielemann F.-K., Korobkin O., Rosswog S., 2015, *ApJ*, 813, 2
- Martínez-Pinedo G., Fischer T., Huther L., 2014, *J. Phys. G Nuc. Phys.*, 41, 044008
- Martínez-Pinedo G., Fischer T., Lohs A., Huther L., 2012, *Phys. Rev. Lett.*, 109, 251104
- McLaughlin G. C., Surman R., 2005, *Nucl. Phys. A*, 758, 189
- Mendoza-Temis J. J., Wu M.-R., Langanke K., Martínez-Pinedo G., Bauswein A., Janka H.-T., 2015, *Phys. Rev. C*, 92, 055805
- Metzger B. D., Bauswein A., Goriely S., Kasen D., 2015, *MNRAS*, 446, 1115
- Metzger B. D., Berger E., 2012, *ApJ*, 746, 48
- Metzger B. D., Fernández R., 2014, *MNRAS*, 441, 3444
- Metzger B. D., Martínez-Pinedo G., Darbha S., Quataert E., Arcones A., Kasen D., Thomas R., Nugent P., Panov I. V., Zinner N. T., 2010, *MNRAS*, 406, 2650
- Metzger B. D., Piro A. L., Quataert E., 2009, *MNRAS*, 396, 304
- Metzger B. D., Thompson T. A., Quataert E., 2007, *ApJ*, 659, 561
- Metzger B. D., Thompson T. A., Quataert E., 2008, *ApJ*, 676, 1130
- Meyer B. S., 1989, *ApJ*, 343, 254
- Meyer B. S., Mathews G. J., Howard W. M., Woosley S. E., Hoffman R. D., 1992, *ApJ*, 399, 656
- Moller P., Nix J. R., Myers W. D., Swiatecki W. J., 1995, *Atom. Data Nucl. Data Tabl.*, 59, 185
- Möller P., Pfeiffer B., Kratz K.-L., 2003, *Phys. Rev. C*, 67, 055802
- Mösta P., Richers S., Ott C. D., Haas R., Piro A. L., Boydston K., Abdikamalov E., Reisswig C., Schnetter E., 2014, *ApJL*, 785, L29
- Nishimura N., Takiwaki T., Thielemann F.-K., 2015, *ApJ*, 810, 109
- Oechslin R., Janka H.-T., 2006, *MNRAS*, 368, 1489
- Perego A., Rosswog S., Cabezon R. M., Korobkin O., Käppeli R., Arcones A., Liebendörfer M., 2014, *MNRAS*, 443, 3134
- Qian Y., Woosley S. E., 1996, *ApJ*, 471, 331
- Qian Y.-Z., 2000, *ApJL*, 534, L67
- Qian Y.-Z., Wasserburg G. J., 2007, *Phys. Rep.*, 442, 237
- Radice D., Galeazzi F., Lippuner J., Roberts L. F., Ott C. D., Rezzolla L., 2016, *MNRAS*, in press, arXiv:1601.02426
- Roberts L. F., Kasen D., Lee W. H., Ramirez-Ruiz E., 2011, *ApJL*, 736, L21
- Roberts L. F., Reddy S., Shen G., 2012, *Phys. Rev. C*, 86, 065803
- Roederer I. U., Lawler J. E., 2012, *ApJ*, 750, 76
- Roederer I. U., Lawler J. E., Sobeck J. S., Beers T. C., Cowan J. J., Frebel A., Ivans I. I., Schatz H., Sneden C., Thompson I. B., 2012, *ApJS*, 203, 27
- Rosswog S., 2015, *Int. J. of Mod. Phys. D*, 24, 1530012
- Sekiguchi Y., Kiuchi K., Kyutoku K., Shibata M., 2015, *Phys. Rev. D*, 91, 064059
- Shakura N. I., Sunyaev R. A., 1973, *A&A*, 24, 337
- Shen S., Cooke R. J., Ramirez-Ruiz E., Madau P., Mayer L., Guedes J., 2015, *ApJ*, 807, 115
- Shibata M., Taniguchi K., 2006, *Phys. Rev. D*, 73, 064027
- Shibata M., Uryū K., 2000, *Phys. Rev. D*, 61, 064001
- Sneden C., Cowan J. J., Gallino R., 2008, *ARA&A*, 46, 241
- Sneden C., et al., 2003, *ApJ*, 591, 936
- Surman R., Caballero O. L., McLaughlin G. C., Just O., Janka H.-T., 2014, *J. Phys. G: Nucl. Part. Phys.*, 41, 044006
- Surman R., McLaughlin G. C., Ruffert M., Janka H.-T., Hix W. R., 2008, *ApJ*, 679, L117
- Tanaka M., 2016, *Adv. Astron.*
- Tanaka M., Hotokezaka K., 2013, *ApJ*, 775, 113
- Tanvir N. R., Levan A. J., Fruchter A. S., Hjorth J., Hounsell R. A., Wiersema K., Tunnicliffe R. L., 2013, *Nature*, 500, 547
- Thielemann F.-K., et al., 2011, *Prog. Part. Nucl. Phys.*, 66, 346
- Thompson T. A., Chang P., Quataert E., 2004, *ApJ*, 611, 380
- Timmes F. X., Swesty F. D., 2000, *ApJS*, 126, 501
- van de Voort F., Quataert E., Hopkins P. F., Kereš D., Faucher-Giguère C.-A., 2015, *MNRAS*, 447, 140
- Vlasov A. D., Metzger B. D., Thompson T. A., 2014, *MNRAS*, 444, 3537
- Wallner A., Faestermann T., Feige J., Feldstein C., Knie K., Korschinek G., Kutschera W., Ofan A., Paul M., Quinto F., Rugel G., Steier P., 2015, *Nature Communications*, 6, 5956
- Wanajo S., Sekiguchi Y., Nishimura N., Kiuchi K., Kyutoku K., Shibata M., 2014, *ApJ*, 789, L39
- Winteler C., Käppeli R., Perego A., Arcones A., Vasset N., Nishimura N., Liebendörfer M., Thielemann F.-K., 2012, *ApJ*, 750, L22
- Woosley S. E., Wilson J. R., Mathews G. J., Hoffman R. D., Meyer B. S., 1994, *ApJ*, 433, 229